Highly Dynamic Shape Memory Alloy Actuator for Fast Moving Soft Robots

Xiaonan Huang, Kitty Kumar, Mohammad K. Jawed, Amir Mohammadi Nasab, Zisheng Ye, Wanliang Shan, and Carmel Majidi*

Shape memory alloys (SMAs) are popular as actuators for soft bioinspired robots because they are naturally compliant, have high work density, and can be operated using miniaturized on-board electronics for power and control. However, SMA actuators typically exhibit limited bandwidth due to the long duration of time required for the alloy to cool down and return to its natural shape and compliance following electrical actuation. This challenge is addressed by constructing SMA-based actuators out of thermally conductive elastomers and examining the influence of electrical current and actuation frequency on blocking force, bending amplitude, and operating temperature. The actuator is composed of a U-shape SMA wire that is sandwiched between layers of stretched and unstretched thermal elastomer. Based on the studies, the ability is demonstrated to create a highly dynamic soft actuator that weighs 3.7 g, generates a force of ≈0.2 N, bends with curvature change of ≈60 m^{-1} in 0.15 s, and can be activated with a frequency above 0.3 Hz with a pair of miniature 3.7 V lithium–polymer batteries. Together, these properties allow the actuator to be used as an "artificial muscle" for a variety of tethered and untethered soft robotic systems capable of fast dynamic locomotion.

1. Introduction

Because they are primarily composed of compliant materials, soft bioinspired robots can exhibit some of the versatility and mechanically robust properties of natural organisms. This includes the ability to resist impact or deformation
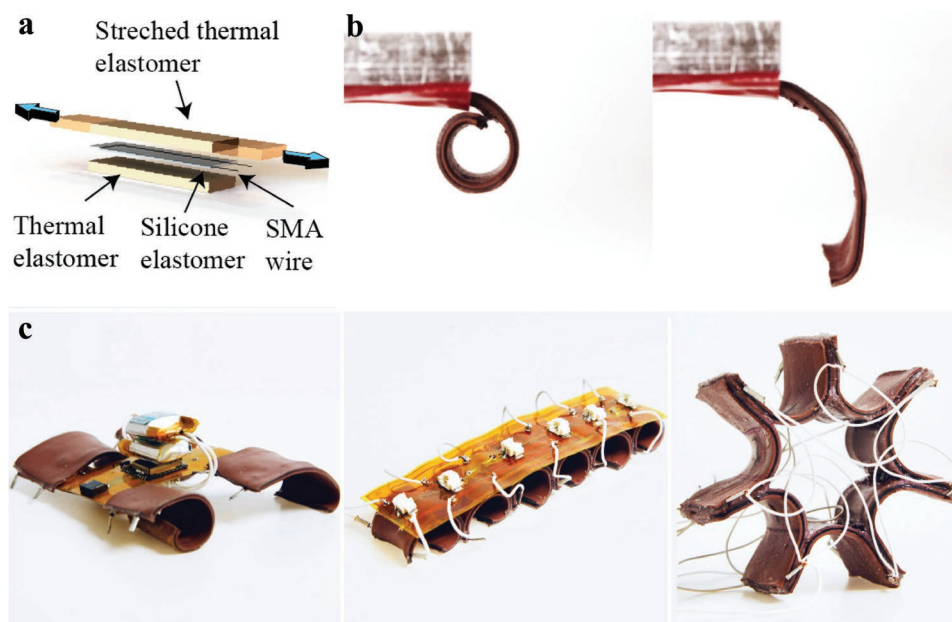
X. Huang, Dr. K. Kumar, Z. Ye, Prof. C. Majidi
Soft Machines Lab
Department of Mechanical Engineering
Carnegie Mellon University
Pittsburgh, PA 15213, USA
E-mail: cmajidi@andrew.cmu.edu
Prof. M. K. Jawed
Mechanical and Aerospace Engineering Department
University of California
Los Angeles, CA 90095, USA
A. Mohammadi Nasab, Prof. W. Shan
Mechanical Engineering
University of Nevada
Reno, NV 89557, USA
Prof. C. Majidi
Robotics Institute
Carnegie Mellon University
Pittsburgh, PA 15213, USA

and maneuver through tightly confined spaces.[1–7] However, soft robot locomotion tends to be relatively slow and typically relies on external hardware for power and control. This is largely due to current limitations with the "artificial muscle" actuators that are used to place the battery-powered electrical motors (e.g., DC motors, servos) that have been traditionally used in robotics. For example, untethered soft robots that use fluidic or dielectric elastomer actuators require bulky on-board hardware for power and control that result in a high payload and slow locomotion speed.[3,8,9] While ionic polymer–metal composites require low voltage and can be controlled using miniaturized electronics, they have not been shown to generate the forces required for a cm-scale robot to walk in dry conditions.[10,11] By contrast, soft robot actuators composed of elastomers embedded with wires or springs of thermally activated smart materials such as shape memory alloy (SMA) can generate large forces in an adequately short time interval and be directly powered and controlled with portable, lightweight electronics.[12] Moreover, they can reversibly transition from being mechanically compliant in their natural (unactuated) state to being stiff and load-bearing when actuated.[12]

Although promising, SMAs have only been used as actuators for untethered soft robot in a limited number of cases.[13,14] A key challenge has been the limited frequency with which SMA-based actuators can be activated. This is due to the long duration of time required for the alloy to cool down and return to its natural shape and compliance following electrical activation. As a result, soft robots powered with SMA actuators either have sudden but infrequent bursts of motion,[14] slow steady-state locomotion gait cycles with long recovery times,[15] tethered hardware[15] or take advantage of marine environments for active cooling.[13,16] In this work, we address this challenge by examining how materials selection, actuator design, and operating conditions can be used to improve the frequency bandwidth of an SMA actuator. In particular, we find that encasing SMA wire in thermally conductive rubber can allow for more rapid heat transfer and enable soft robots to exhibit robust dynamical motion over extended operating times (**Figure 1**a). The SMA actuator is capable of a rapid transition
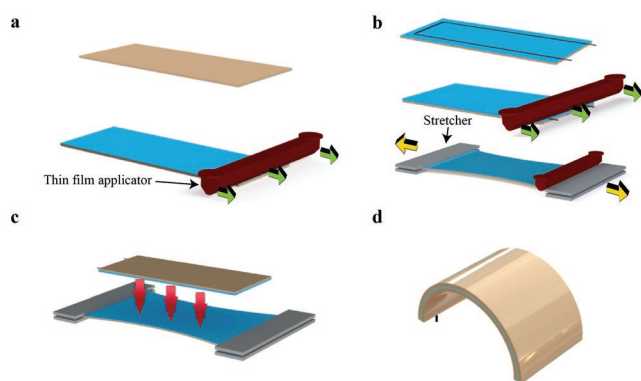
Figure 1. a) Layup of the highly dynamic shape memory alloy (SMA)-based actuator. b) Optical photographs showing the actuator in a relaxed (left) and actuated (right) state. c) Implementation of the highly dynamic soft actuators in various soft robotic testbeds: untethered soft quadruped, caterpillar inspired untethered soft robot, and soft rolling robot.

between a soft curled unactuated state and a rigid straight-like actuated state (Figure 1b). Electrical current supplied by a pair of 3.7 V lithium–polymer (LiPo) batteries for a duration of 0.15 s is enough to propel the actuator into the air and leap forward (Figure 1c). This dynamic response has enabled the SMA actuator to be used to improve locomotion speed in a variety of recent soft robot implementations, including the untethered quadruped, caterpillar-inspired robot, and rolling robot shown in Figure 1d.

Harnessing the dynamics of SMA actuation for continuous, steady-state, soft robot locomotion requires careful study of the trade-offs between input current, recovery time activation cycles, force output, and actuation frequency. In this study, we examine the key factors that govern the design and operation of SMA-based soft robot limb actuators: (i) elastomer selection (which influences elastic modulus and thermal conductivity), (ii) elastomer layer dimensions (length, width, thickness), (iii) elastomer prestretch and corresponding natural (nonactuated) bending curvature, (iv) SMA wire diameter, (v) electrical current/power delivered to SMA wire during actuation, (vi) duration of SMA activation, and (vii) cooling time; the minimum duration of time between actuation cycles. Items (i), (ii), and (iv) were selected so that the actuator could support the weight of a centimeter-scaled robot of weight ≈30 g. To better understand the influence of the remaining properties, we performed a series of characterization studies that examined the bending response and blocking force of individual actuator. In addition to furnishing insights to inform SMA-based limb design, these studies provide independent evidence that the proposed materials architecture is capable of producing the motion, force outputs, and actuation frequencies required for different types of locomotion in soft robotics systems.

2. Fabrication

To fabricate the actuator, we first prepare two rectangular sheets of thermally conductive elastomer (H48-2, thermal conductivity: 2.2 W m^{-1} K^{-1}, tensile strength: 700 kPa, and hardness: Shore 10A, T-Global) with dimensions of 55 × 22 × 0.5 mm and 70 × 37 × 0.5 mm, respectively. The elastomer sheets are cut using a CO_2 laser cutting system (30W VLS 3.50; Universal Laser Systems). Next, we bend the SMA wire (0.3 mm in diameter; resistance of 12.2 Ω m^{-1}, Dynalloy) into a U-shape with a dimension of 55 × 13 mm with pliers. The wire is bonded to the sheets with silicone elastomer (Ecoflex 00–30, Smooth-On), which is prepared by mixing prepolymer at a 1:1 ratio by mass in a planetary centrifugal mixer (AR-100, THINKY) and deposited on the smaller rectangular thermal tape using a thin-film applicator at a nominal thickness of 0.2 mm (**Figure 2**a). The thermal tape with the uncured silicone is placed in an oven at 50 °C for 7 min to become half-cured. While waiting for the elastomer to be half-cured, the larger laser-cut thermal tape is stretched to a prescribed strain using a linear stretcher (A150602-S1.5, Velmex) for ten times to remove any residual stresses or inelasticity associated with the Mullin's effect. Next, we take out the thermal elastomer with half-cured silicone from the oven and place the bent SMA wire on the top. Then another layer of the uncured silicone with a thickness of 0.4 mm is applied on the top of the SMA wire. At the same time, we apply a layer of 0.1 mm uncured silicone on the top of the prestretched large tape (Figure 2b). Both thermally conductive elastomer with silicone layers are placed in the oven at 50 °C for 7 min to become half-cured and then clamped together with two binder clips (Figure 2c). Finally, we place the bonded actuator back into the oven at 50 °C for 10 min to fully cure it and cut it out along the outline of the smaller tape with a pair of scissors after cured (Figure 2d).

**ADVANCED
SCIENCE NEWS**
www.advancedsciencenews.com

**ADVANCED
MATERIALS
TECHNOLOGIES**
www.advmattechnol.de

Figure 2. Schematic showing various steps involved in the fabrication of the actuator. a) Apply a 200 µm thick silicone (Ecoflex 30) layer on the top of the 55 × 22 × 0.5 mm thermally conducting elastic tape using a thin film applicator (red). b) Place SMA wire on top of the partially cured silicone and apply a 400 and 100 µm thick Ecoflex 30 layer on top of the 55 × 22 × 0.5 mm thermal tape and a prestretched 70 × 37 × 0.5 mm laser-cut layer of thermal tape, respectively. c) Bond the two thermal tape layers together. d) Cut out the actuator after it is fully cured.

3. Actuator Characterization

We begin by characterizing the flexural and blocking force properties of the individual SMA actuator. The flexural stiffness $D = M/\Delta\kappa$ is defined by the change in bending curvature

$(\Delta\kappa)$ induced by an internal bending moment (M) and is calculated by analyzing results from experimental testing. The analysis utilizes computational methods based on discrete differential geometry[17] to relate the global loading conditions with internal bending moment. Next, blocking force experiments are performed to determine the actuator response rate and force output as a function of applied current and internal residual strains. The reliability of actuated motion in terms of actuator–curvature variation due to accumulated heat is studied both computationally and experimentally for different actuation schemes over 150 cycles.

3.1. Flexural Response

The goal of the flexural response analysis is to (i) relate material layup, flexural response, and electrical activation, and (ii) study the effect of heat accumulation on the actuated response over extended operating times. As shown in **Figure 3**a (orange box) and discussed in the Experimental Section, the actuator has a natural (relaxed) curvature, κ_n, that scales with the amount of prestretch applied to the top layer of thermally conductive elastomer (H48-2, T-Global) when it is bonded to the bottom layer. When powered with electrical current for an activation time of t_a, the actuator transitions from a soft, curved state (orange box in Figure 3a) to a stiff, straight state (green box in Figure 3a). The following three subsections describe characterization
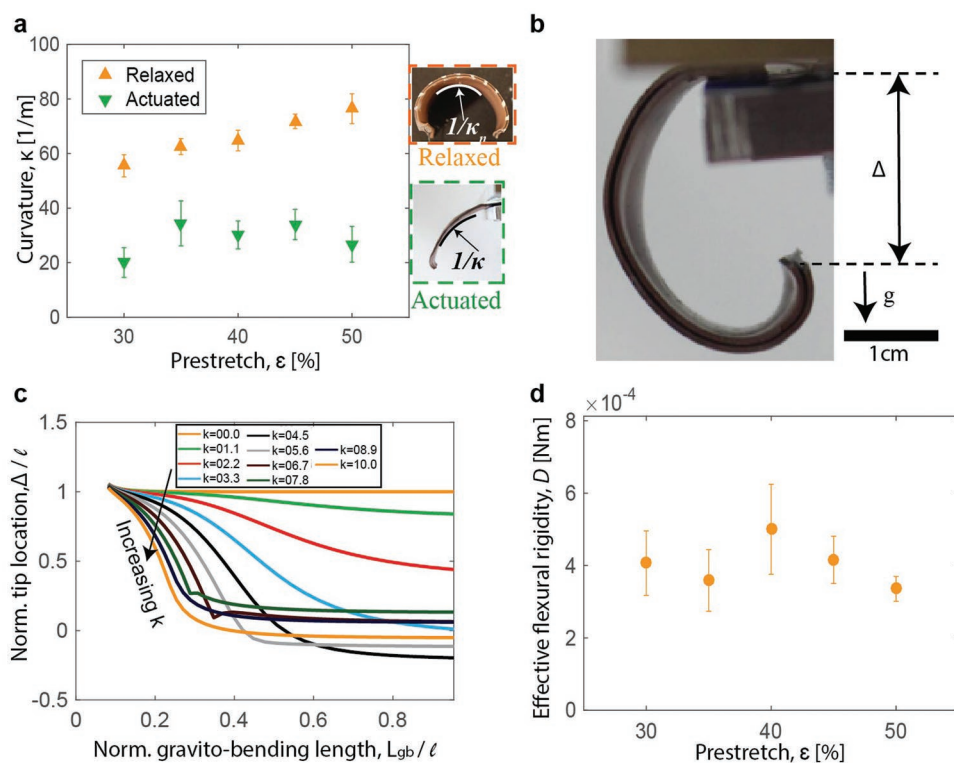
Figure 3. a) Plot of curvature of the actuator in relaxed (κ_n) and actuated state (κ) as the function of prestretch of the top layer of thermally conducting elastomer tape. Optical photograph of an actuator in a relaxed (orange box) and activated state (green box) are shown as insets. b) Image of the experimental setup for measuring actuator tip displacement, Δ, in order to determine the flexural stiffness with DER (Δ is the vertical distance between the clamped point and the free-end of the actuator). c) Look-up plot for computing flexural stiffness from Δ and normalized curvature k. d) Plot of effective flexural stiffness (in the passive, nonactivated state) as a function of prestretch.

1800540 (3 of 9)

of the mechanical properties and response of the actuator in its actuated and unactuated states. For these experiments, we have limited elastomer prestretch to a range of 30% ≤ ε ≤ 50% in order to achieve natural bending curvatures that are appropriate to implement actuator into various soft robotic configurations shown in Figure 1. When the prestretch is too small (ε < 30%), we found that the antagonistic force exerted by the prestretched layer is inadequate to achieve significant change in the curvature. Likewise, for a prestretch larger than 50%, we observe that the actuator makes self-contact and cannot support the motion of the robotic testbeds.

3.1.1. Influence of Prestretch on Natural Curvature

We determine the natural curvature of the actuator (κ_n) by assuming constant curvature and fitting the actuator shape to a circular arc (orange box in Figure 3a,). Prior to this measurement, actuators are activated five consecutive times to eliminate any residual inelasticity associated with a "Mullins effect" of the thermally conductive elastomer. Following each actuation signal for actuation time $t_a = 1$ s, the actuator remains unpowered for cooling time $t_c = 1$ min, sufficient to cool it down to room temperature. We also measure the curvature in the actuated state (κ) following a similar methodology (green box in Figure 3a). For this case, a current of 2.5A is applied through the SMA wire for an actuation time of $t_a = 2$ s, long enough to activate it and transform the Ni–Ti alloy from the martensite to austenite phase. The curvature in the actuated state is measured while the actuator is hanging under gravity, although we expect the effect of gravity to be negligible due to enhanced mechanical stiffness upon actuation. Figure 3a shows the curvature of the actuator in both states as a function of the prestretch, ε, applied to the bottom layer of the thermally conducting elastomer tape. The relaxed natural curvature increases significantly with the prestretch while the actuated state sees significantly less variation. When the SMA wire is at room temperature, it exhibits negligible stiffness. Therefore, the antagonistic forces exerted by the prestretched layer and the nonstretched layer will govern the flexural deformation. These forces increase with prestretch, which causes the actuator to naturally bend into a more curled shape. However, the SMA wire becomes significantly stiffer when it is completely actuated (in austenite phase) and overwhelms the elastic restoring forces of the soft tape. This allows the actuator to assume a less curled configuration ($\kappa \approx 20$ m^{-1} in a 5 cm long actuator) with statistically insignificant influence from prestretch, as shown in Figure 3a.

3.1.2. Flexural Stiffness

Having characterized the shape of the actuator, we proceed to examine its flexural stiffness. For the elastomer limb with embedded SMA wire, the flexural stiffness D can be estimated by summing the product EJ for each material element, where E and J are the elastic modulus and cross-sectional area moment of inertia, respectively. Due to the presence of the SMA wire, the actuator is treated as flexible but inextensible. We, therefore, focus on quantifying the flexural stiffness of the actuator
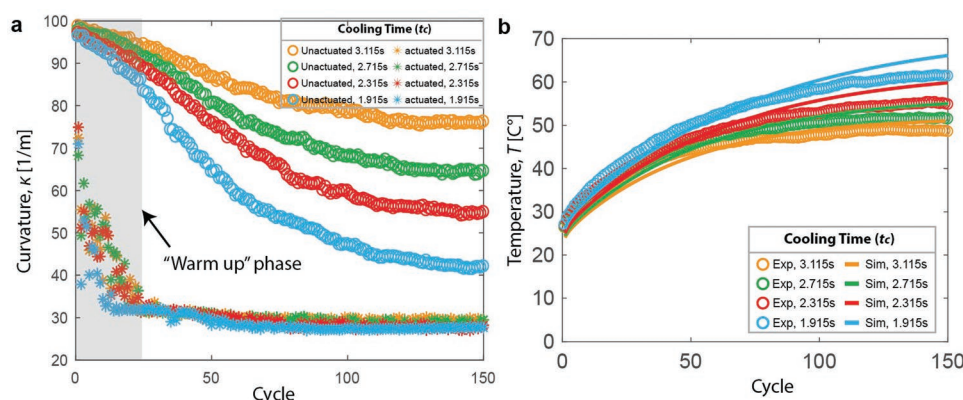
at different values of the prestretch. This is accomplished using a semiempirical technique that combines experimental measurements with calculations performed using the discrete elastic rods (DER; see Section S1, Supporting Information) computational framework.[17,18] The purpose of using DER is to relate measurements of passive deflection of the actuator under gravitational loading (Figure 3b) with flexural stiffness and establish a mapping (i.e., "look up" plot) between length, vertical deflection, and stiffness (Figure 3c). Details of this method for calculating D are presented in the Experimental Section. Figure 3d shows the flexural stiffness of our actuators in the unactuated state obtained using this method as a function of the prestretch. We observe a nonmonotonic but statistically insignificant variation in stiffness that is likely due to the nonlinearity and hysteresis in the mechanical behavior of the thermally conductive elastomer (Figure S1, Supporting Information) and SMA wire. Furthermore, the variation in the flexural stiffness is relatively modest as the prestretch is increased from 30% to 50%.

In order to achieve actuation with both adequate displacement and load-bearing, we are primarily interested in actuators that combine greater change in curvature between nonactuated and actuated states with higher stiffness of the structure. Based on our findings on the influence of prestretch on change in the curvature (Figure 3a) and flexural stiffness (Figure 3d) of the actuator, we chose to use a prestretch of 50% since such actuators exhibit the maximum change in curvature upon actuation and retain a flexural stiffness similar to other actuators in our preferred range of prestretch.

3.1.3. Cyclical Loading and Influence of Activation Frequency

To examine the reproducibility of the actuated motion over extended operating times, we capture the maximum actuated curvature and nonactuated curvature at the end of each cycle of an actuator (ε = 50%) for 150 actuation cycles at different cooling times and present these two curvatures for each cycle. In all cases considered here, we use a current of 4.1–4.3 A powered from a pair of LiPo batteries (3.7 V, 100 mAh; Lectron) that are connected in series for an activation time of $t_a = 0.105$ s, and then turned off for a cooling time of t_c (1.915, 2.315, 2.715, 3.115 s). This actuation scheme is performed with an on-board microcontroller (RFD22301; RFduino) and transistor (A03416; Alpha & Omega Semiconductor). As before, the shape of the actuator can be estimated to be a circle with a curvature κ that varies with time. The temperature of the SMA wire is measured at the end of each cycle by embedding a thermistor into the actuator (see Figure S2, Supporting Information). The actuator is within a "warm up" phase for the first ≈10–25 cycles and both actuated and unactuated curvature is observed to decrease (**Figure 4**a). The actuated curvature decreases faster than the unactuated curvature, which leads to a greater curvature difference between the actuated and the unactuated states. This may be attributed to a gradual increase in the average baseline temperature of the actuator as trapped heat accumulates within the elastomer surrounding the SMA wire. Such a temperature increase reduces the thermal energy barrier for martensite (M_f)-to-austenite transition (A_s) and allows for more material to undergo crystalline phase change, resulting in greater actuator straightening during

**ADVANCED
SCIENCE NEWS**

www.advancedsciencenews.com

**ADVANCED
MATERIALS
TECHNOLOGIES**

www.advmattechnol.de

Figure 4. a) Plot of curvature measured at the beginning and end of each cycle for 150 cycles under various cooling time. b) Plot of measured and simulated temperature at the end of each cycle for 150 cycles under various cooling time.

activation. Moreover, in the unactuated state, the actuator—although steadily increasing in temperature—returns to an almost completely martensitic state in which the flexural stiffness is low and the natural bending curvature remains high.

After this warm up stage, the actuated curvature stops increasing, which indicates that the SMA wire completely transitions to the austenite phase within each cycle. The unactuated curvature continues to gradually increase since the accumulated heat causes the increase of the baseline temperature, which prevents portions of the alloy to transition back to the martensite phase. Because the wire becomes stiffer in this unactuated state, the elastic restoring force from the prestretched layer cannot bend the actuator back to its initial curvature, resulting in an increase in unactuated curvature for the subsequent loading cycle. For longer cooling times (e.g., $t_c = 3.115$ s), the unactuated curvature appears to approach steady state after ≈100 loading cycles. For shorter cooling times, the increase of the unactuated curvature appears to continue past 100 cycles.

3.1.4. Thermal Analysis

To determine whether the results in Figure 4a could be explained by changes in baseline temperature, we performed experimental and numerical thermal analysis during cyclical activation. Experimental measurements were performed by placing a thermistor (ERT – J0ET102J, Panasonic) above the SMA wire, as illustrated in Figure S2 of the Supporting Information. Because there is silicone elastomer between the thermistor and wire, this measurement approach will not get precise values for the internal temperature of the SMA or enable determination of when phase transition will occur (i.e., when T exceeds or drops below A_s or M_f, respectively). Instead, it provides an estimate for the average, baseline temperature of the actuator discussed in the previous subsection. Referring to Figure 4b, this baseline temperature is observed to increase steadily during cyclical activation. As was shown for measurements of curvature, steady state is achieved after ≈100 cycles for a cooling time $t_c = 3.115$ s. The temperature increases more steeply as t_c decreases. Together, these results provide evidence that the decrease of the unactuated curvature during cyclical activation is indeed governed by the increase of baseline temperature and its influence from cooling time.

To further examine the effects of cyclical activation and cooling time on baseline temperature, a 3D numerical thermal analysis is performed to predict temperature near the SMA wire for different values of input power, t_a, t_c, and number of cycles (see "Finite Element Modeling" in the Experimental Section for details). Here, the thermal analysis is decoupled from the kinematic response of the actuator and a quarter model of a straight actuator is used to find the temperature at different locations of the model. To incorporate the effect of the actuator motion in the thermal analysis, an enhanced coefficient of heat transfer, 10 W m⁻² K⁻¹, for convection is considered. In this model, the internal heat generation in the SMA wire as a function of the applied electrical current during t_a and t_c is obtained from

$$\dot{q}_{in_{ta}} = I^2 R - f_1 \frac{L_h}{t_a} - w_m \text{ and } \dot{q}_{in_{tc}} = f_2 \frac{L_h}{t_c} \tag{1}$$

where R, I, f_1, f_2, L_h, and w_m are the wire resistance, the applied electrical current, the portion of the SMA material transitioning from martensite to austenite during t_a, the portion of the material transitioning from austenite to martensite during t_c, the latent heat of phase transformation of the SMA material, and the mechanical work done by the actuator during t_a, respectively. The mechanical work was neglected in our calculations. In order to simplify the model, we considered the values of f_1 and f_2 to be unity. Figure S4 of the Supporting Information shows a schematic of the thermal model used to simulate the temperature distribution in a 3D quarter model of a straight SMA-based actuator. A convection heat transfer boundary condition was imposed to the surfaces of the actuator exposed to the air. Also, the interfaces between the wire, silicone interface (Ecoflex 30), and the thermally conductive elastomer were modeled as perfectly bonded.

The results of the numerical simulation are plotted in Figure 4b and compared with the experimental measurements without the aid of data fitting. While the agreement looks reasonable, we should note that the simulation calculations are for the temperature at the start of each cycle just before the 0.105 s pulse of current is supplied (i.e., during the current pulse the predicted temperature will be momentarily higher). Nonetheless, we think this comparison is fair given that there is elastomer between the thermocouple and wire and so an actual temperature spike within the SMA is unlikely to be measured. Also, to

simplify the simulation, it was assumed that in each cycle all the elements of the SMA wire transition from martensite to austenite during t_a and from austenite to martensite during t_c. Since a pair of batteries was used to provide the power, the current/voltage of the battery dropped for the final cycles of the operation, so the heating power decreased. However, a fixed current of 4.1 A was applied to the actuator in the numerical model, which might be the reason why the simulation over predicts the temperature compared with experiments near to the final cycles of operation.

3.2. Blocking Force

When the actuators are implemented on soft robotic test-beds like the quadruped and soft caterpillar robots shown in Figure 1d, the changes in shape of the actuated actuator enable these robots to achieve a net forward propulsive motion. The force exerted by the SMA-powered actuator on the ground needs to overcome frictional force and gravity. To examine this, we perform blocking force tests using the load cell on a materials testing system (Instron 5969). Our objective with these tests is to characterize actuator force output as a function of the design parameters (e.g., prestretch) and operational input (e.g., magnitude of current in SMA). In order to evaluate the force exerted by the actuator, we consider a simplified setup illustrated in **Figure 5**a, which comprises of a rigid force plate fixed on a 10 N load cell and with an actuator clamped at one end. The distance between the force plate and the clamped end is adjusted such that the actuator in the relaxed state just touches the force plate. During each experimental trial, an actuator is repeatedly actuated ≈102 times through direct Joule heating with an activation time t_a of 0.15 s and cooling time t_c of 8.0 s. The actuator in its actuated state tries to straighten out but is blocked by the rigid force plate, with corresponding blocking force registered by the load cell (Figure 5a).

3.2.1. Influence of Prestretch on Blocking Force

We measure the variation in the blocking force from the actuator with prestretch for selected values of activation current (Figure 5b). The blocking force slightly decreases with increasing prestretch, which can be understood from the competition between the antagonistic force in the thermal tape layers and the stiffness of the activated SMA wire. As the prestretch increases, the antagonistic force in the two soft layers arising from the strain mismatch also increases. In order for the actuator to straighten, the residual stresses from this mismatch must be overcame by the bending and stiffness of the activated SMA wire. However, the increase in stiffness ΔD caused by SMA activation decreases with increasing prestretch and, as a result, the blocking force also decreases. However, for a residual strain ε, the blocking force significantly increases with the applied electrical current. As shown in Figure 5b, as the current is increased from 3.4 to 4.3 A, there is an approximately threefold increase in blocking force for any given value of ε. With higher current, more Ni–Ti alloy changes from the martensite to austenite phase and results in greater flexural stiffness and curvature change. Because the load cell prevents the actuator from bending, this combination of increased flexural stiffness and deflection results in a significant increase in blocking force. During the operation of the robot, we applied a current of 4–4.3 A since it was found to produce push-off force above 0.14 N between the limb and the force plate that is adequate to propel forward ≈30 g soft robot including on-board electronics and controls.

3.2.2. Cyclical Loading and Influence of Activation Frequency

To examine the relationship between the actuated force, actuation cycles, and cooling time, we capture the blocking force of an actuator ($\varepsilon = 50\%$) for 150 actuation cycles at different cooling times by using the same setup. The same circuit and battery that were used for curvature cyclic loading experiment are also used here. The temperature of the SMA wire at the end of each cycle is also measured by the same method. The blocking force reaches a steady state value between 0.14 and 0.17 N after the warm up phase and we do not see significant difference in the stabilized blocking force as the cooling time varies. The trend of the temperature change shown in Figure 5c is very similar to Figure 4b except the absolute temperature
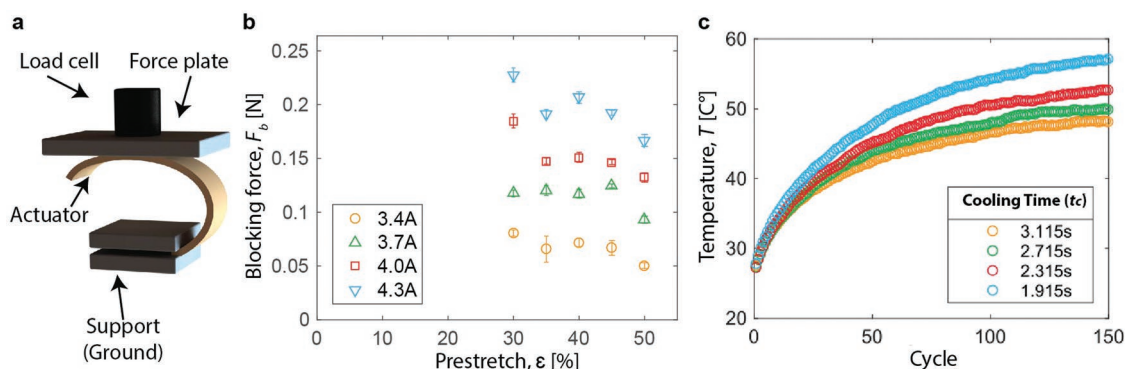
Figure 5. a) Schematic layout of the experimental setup for measuring the blocking force (F_b). The actuator is cyclically activated with electrical current and then allowed to cool. Force is recorded using the load cell of an Instron 5969. b) Plot of blocking force versus prestretch for various applied currents. c) Plot of temperature of the SMA wire measured at the end of each cycle for 150 cycles with various cooling times when the actuator is clamped on the instron plate for blocking force measurements.

1800540 (6 of 9)

**ADVANCED
SCIENCE NEWS**
www.advancedsciencenews.com

**ADVANCED
MATERIALS
TECHNOLOGIES**
www.advmattechnol.de

is lower due to the heat conduction from the actuator to the blocking force plate.

4. Discussion

In this study, we presented the design and fabrication method for highly dynamic SMA actuators that achieve a blocking force of ≈0.2 N and a curvature change of ≈60 m^{-1} in 0.15 s. The actuator requires 7.4 V to be driven and ≈3 s to consistently switch between actuated and unactuated states. The design utilizes (i) the mismatch of the strain between the prestretched and the unstretched elastic tape layers coupled with the difference in rigidity between martensite and austenite phases of the embedded SMA wire and (ii) high thermal conductivity of the elatomeric tapes to produce fast dynamic response over a longer duration of time. Together, the properties of the SMA-based soft robot actuator make it a promising candidate for implementation in untethered and fast moving robots. A single actuator can be implemented as a tethered jumping robot that can jump over an obstacle of 9.4 mm height. By generating a force of ≈0.2 N in a short amount of time (≈0.1 s), the actuator can produce a propulsive thrust that causes the robot to leap over the obstacle (**Figure 6**). The antagonistic force generated by the prestretch layer causes the actuator to rapidly curl back to its curved configuration so that it is ready for the next jump.

In the actuator characterization, we show that a 50% elastomer prestretch provides maximum change in the curvature of the actuator without exhibiting self-contact. Moreover, we found that selecting a higher prestretch has no significant influence on flexural stiffness or blocking force. As expected, we observed that the curvature of the actuator in its relaxed (natural) state increases significantly with the prestretch applied to the top layer of thermal tape. However, the curvature in the actuated state is only slightly larger for actuators with larger original prestretch. This is because in the actuated state, the bending curvature is governed by the straightening of the heated SMA wire and the flexural stiffness and natural shape of the surrounding elastomer has only limited influence.

According to our studies, the influence of prestretch on flexural stiffness (D) and blocking force (F_b) are modest. The slight dependence of D on prestretch is observed to be nonmonotonic, which is likely due to the nonlinearity and hysteresis of the thermal tape. The blocking force slightly decreases with the prestretch time due to the increasing antagonistic force from the prestretch tape. However, it increases significantly with increasing electrical input. The blocking force corresponds to the normal force applied by the limb to the ground and relates to the force necessary for the robot to overcome gravity and propel forward. For the selected prestretch, force is observed to increase by a factor of 2.4 when the applied electrical current actuation increases from 3.4 to 4.3A. Limb activation with a higher current resulting in greater force because more of the Ni–Ti alloy transforms from the relatively soft twinned martensite phase to the rigid and more load-bearing austenite phase.

Although this work focuses on a specific actuator layup, more general designs of SMA-based actuators for fast moving soft robots can build on the following key insights from the present study: (i) embedding SMA wire with elastomer that has high thermal conductivity can enable accelerated heat dissipation, reduce the cooling time, and thus increase the bandwidth of the SMA actuator. (ii) Activating the SMA with a high electrical current in a short amount of time enables rapid actuation and the generation of a large push-off force, thereby allowing the robot to achieve fast locomotion. (iii) Prestretching one of the layers of thermal tape prior to bonding gives the actuators natural curvature and allows them to function as load-bearing limbs capable of carrying the weight of the robot's electronics, battery, and frame. The prestretch also introduces antagonistic forces that help the actuator rapidly transition back from the straightened actuated state to the curled unactuated state, thereby improving the actuation frequency. However, the prestretch strain needs to be carefully selected since large prestretch can lead to self-contact and reduced blocking force, while small prestretch would reduce the antagonistic force, resulting in increased relaxation time or even the inability for the actuator to transition back to a curled unactuated state. (iv) Lastly, this study suggests that computational tools for like DER that model elastic rod deformation can be useful for characterizing the properties of soft compliant actuators. More generally, DER could potentially play a more important role in modeling and designing soft robots that are composed of soft slender actuators. Such models could reduce the need for iterative experimental implementations or trial and error design. Future improvement also include improving the control scheme to prevent the actuator from overheating and increase actuation frequency; modifying the design to enable the actuator to achieve various actuation mode in a 3D space; and integration of built-in soft strain sensors to monitor limb curvature during locomotion.
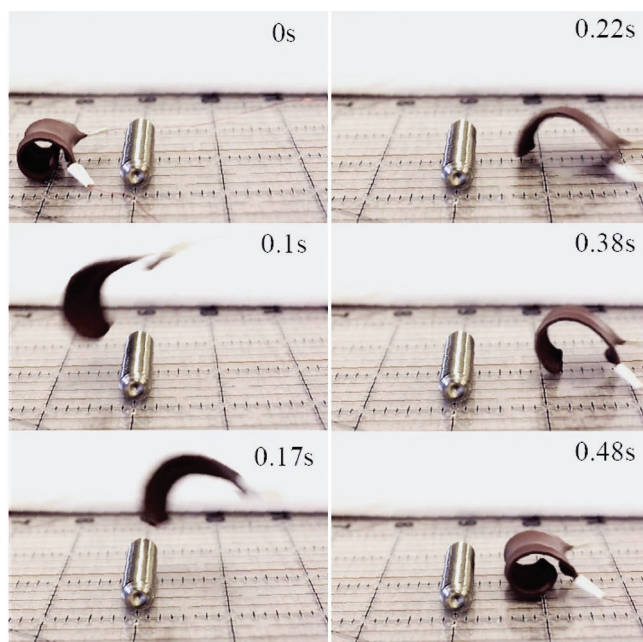
Figure 6. Composite of video frames showing tethered single jumper fabricated with the actuator jumping over an obstacle (height: 9.74 mm).

5. Conclusion

In summary, we combine SMA wire and thermally conductive elastomer to create a lightweight (3.7 g) and highly dynamic actuator for mobile soft robots. The SMA-based compliant actuator can reversely transition between the compliant unactuated and stiff actuated states with a frequency of ≈0.3 Hz and generate a force of 0.2 N in ≈0.15 s. It is powered by a pair of miniature 3.7 V LiPo batteries that can be incorporated into the body of a soft robot without adding significant bulk. In this respect, the actuator present here can be driven by on-board control electronics and power and provide enough force and actuation frequency required for fast locomotion of an untethered, centimeter-scale soft robots. While the study focused on a specific actuator layup, the experimental characterization and theoretical modeling led to general insights could inform the design of other SMA-based soft robot actuators.

6. Experimental Section

The actuator characterization was performed on actuators with prestretch ranging from 30% to 50% (in increments of 5%). For each prestretch, the reported values of curvature, and blocking force were measured for four separate testing samples.

Curvature Measurement: Prior to the curvature measurement, all actuators were activated for five times to eliminate any Mullins effect, and after each actuation, the actuator was relaxed for 1 min to cool it down to the room temperature. To measure curvature of the actuator in the relaxed state, the actuator was placed flat on the bench-top and the curvature was estimated by fitting the shape of actuator to a circle of constant curvature, κ_n. Curvature measurement in the activated state κ was made by hanging the actuator under gravity using a custom-designed holder and activating it by applying a current of 2.5 A for 2 s. The holder was designed to allow the actuator to move unobstructed upon activation. The curvature in the actuated state was measured using the same methodology as in the relaxed state. For the cyclic loading, the actuator was hang by the holder and powered by a pair of 3.7 V LiPo batteries connected in series for 0.105 s and cooled down for a cooling time t_c (1.915, 2.315, 2.715, and 3.115 s), controlled by a microcontroller (RFD22301, RFDUINO). The curvature was measured right before the actuation of the actuator using the same methodology.

Flexural Rigidity: For this analysis, the actuator was treated as an elastic rod with uniform stiffness along the length. The flexural stiffness was then estimated from comparing the experimentally measured shape under gravity with what would be predicted for an elastic plate. Due to the relatively large bending angles, a linearized Euler–Bernoulli beam theory could not be used. Instead, the actuator was modeled as a Cosserat rod and DER was employed to analyze deflection. Figure 3b shows a photograph of the setup where an actuator is clamped at one end and allowed to hang under gravity. Referring to the figure, the tip displacement, Δ, which is defined as the vertical distance between the clamped point and the free-end of the actuator was measured. An effective flexural stiffness could now be determined from the natural curvature (κ_n), tip displacement, and the physical parameters (density, length, and width) of the actuator. DER was used to quantify Δ as a function of the gravitobending length,[19,20] Lgb, at various values of natural curvature. From a scaling between bending and gravitational energies, it follows that Lgb = $[Db/(\rho g)]1/3$, where D is the plate flexural stiffness, b is the width, and ρ is the mass per length. In Figure 3c, the tip displacement as a function of gravitobending length (normalized by the length of the actuator) is plotted. The legend shows the corresponding normalized natural curvature, $k = \kappa_n/l$, where l is the length of the actuator. This can be treated as a look-up table to compute flexural stiffness from Δ and k. That is, the Δ versus Lgb curve is selected

that corresponds to the natural curvature of the actuator in question, the gravitobending length from the measured tip displacement is obtained, and the flexural stiffness using the expression for Lgb is computed.

Blocking Force Measurement: The blocking force applied by each actuator was measured at four different values of activation current: 3.4, 3.7, 4.0, and 4.3 A. The activation current below 3.4 A did not provide enough Joule heating to actuate SMA whereas, the current above 4.3 A resulted in overheating and permanent deformation of the SMA wire. The blocking measurements were made using a mechanical testing machine (Instron 5969) with the setup shown in Figure 5a. To begin, the distance between the clamped end and the force plate was adjusted such that the actuator in relaxed state just touched the force plate attached to the load cell. Next, the actuator was activated repeatedly for ≈10^2 times by applying current with the above values for 0.15 s in each actuation cycle with the cooling time of 8.0 s. The force exerted by the limb on the load cell was automatically recorded for the duration of the 10^2 actuation cycles. For the cyclic loading, the same setup was used to measure the blocking force and the actuator is powered by a pair of 3.7 V LiPo batteries connected in series for 0.105 s and cooled down for a cooling time t_c (1.915, 2.315, 2.715, and 3.115 s), controlled by a microcontroller (RFD22301, RFduino).

Temperature Measurement: A thermistor (ERT – J0ET102J, Panasonic) was glued on the top of the SMA wire by a thermal adhesive (Arctic Silver Alumina) before the fabrication of the actuator. In the cyclic test, the thermistor was connected in series with a resistor (1000 Ω) and split 5 V with it. The voltage added on the thermistor was read at the end of each cycle for five times at an interval of 10 ms. The average voltage value is used and the average resistance of the thermistor is calculated by using $R_t = V_t/(5 - V_t) \times R$, where R_t is the resistance of the thermistor, V_t is the average value of the voltage add on the thermistor, and R is the resistor connected in series with the thermistor. Then a simplified version of the Steinhart–Hart equation is used to calculate the temperature: $T_t^{-1} = T_0^{-1} + B^{-1} \times \ln(R_t/R_0)$, where T_t is the temperature of the spot that the thermistor was placed on the SMA wire, T_0 is 298.15 K, B is the coefficient of thermistor (4450 in this case), R_t is the resistance of the thermistor, and R_0 is the resistance of thermistor at 298.15 K.

Finite Element Modeling: ANSYS Workbench 18.1 finite element modeling was used to calculate the full transient temperature profile in the 3D quarter model of a straight actuator. Since the simulations results agree well with the experimental data, the coupled structural–thermal analysis was not performed. In this simplified model, internal heat was generated along the SMA wire and a convection heat transfer boundary condition was imposed on the surfaces of the actuator exposed to the air. The interfaces between the wire, Ecoflex, and the thermal tape parts were modeled as perfectly bonded. The appropriate element types (SOLID87, SURF152, TARGET170, and CONTA174) based on the location of the cell—, i.e., whether it is an internal element, a contact element, or a surface element were selected. Material properties for transient thermal modeling were set according to materials data sheet and literature values. Heat capacity, thermal conductivity, and mass density were considered to be 1050 J kg^{-1} K^{-1}, 0.2 W m^{-1} K^{-1}, and 1070 kg m^{-3} for Ecoflex 30, 837.4 J kg^{-1} K^{-1}, 18 W m^{-1} K^{-1}, and 6450 kg m^{-3} for SMA wire, and 1000 J kg^{-1} K^{-1}, 2.2 W m^{-1} K^{-1}, and 2430 kg m^{-3} for thermally conducting elastomer, respectively.

Supporting Information

Supporting Information is available from the Wiley Online Library or from the author.

Conflict of Interest

The authors declare no conflict of interest.

Keywords

computational modeling, dynamic actuators, shape memory alloy, soft robotics

[1] C. Majidi, *Soft Rob.* **2014**, *1*, 5.
[2] S. Kim, C. Laschi, B. Trimmer, *Trends Biotechnol.* **2013**, *31*, 287.
[3] D. Rus, M. T. Tolley, *Nature* **2015**, *521*, 467.
[4] D. Trivedi, C. D. Rahn, W. M. Kier, I. D. Walker, *Appl. Bionics Biomech.* **2008**, *5*, 99.
[5] C. Laschi, B. Mazzolai, M. Cianchetti, *Sci. Rob.* **2016**, *1*, eaah3690.
[6] R. Pfeifer, M. Lungarella, F. Iida, *Commun. ACM* **2012**, *55*, 76.
[7] S. I. Rich, R. J. Wood, C. Majidi, *Nat. Electron.* **2018**, *1*, 102.
[8] A. O'Halloran, F. O'Malley, P. McHugh, *J. Appl. Phys.* **2008**, *104*, 071101.
[9] A. D. Marchese, C. D. Onal, D. Rus, *Soft Rob.* **2014**, *1*, 75.
[10] M. Shahinpoor, Y. Bar-Cohen, J. O. Simpson, J. Smith, *Smart Mater. Struct.* **1998**, *7*, R15.
[11] C. Jo, D. Pugal, I. K. Oh, K. J. Kim, K. Asaka, *Prog. Polym. Sci.* **2013**, *38*, 1037.
[12] J. Mohd Jani, M. Leary, A. Subic, M. A. Gibson, *Mater. Design* **2014**, *56*, 1078.
[13] Z. Wang, G. Hang, J. Li, Y. Wang, K. Xiao, *Sens. Actuators, A* **2008**, *144*, 354.
[14] H.-T. Lin, G. G. Leisk, B. Trimmer, *Bioinspiration Biomimetics* **2011**, *6*, 026007.
[15] S. Mao, E. Dong, H. Jin, M. Xu, S. Zhang, J. Yang, K. H. Low, *J. Bionic Eng.* **2014**, *11*, 400.
[16] M. D. Bartlett, N. Kazem, M. J. Powell-Palm, X. Huang, W. Sun, J. A. Malen, C. Majidi, *Proc. Natl. Acad. Sci. USA* **2017**, *114*, 2143.
[17] M. Bergou, M. Wardetzky, S. Robinson, B. Audoly, E. Grinspun, *ACM Trans. Graphics* **2008**, *27*, 1.
[18] M. Bergou, B. Audoly, E. Vouga, M. Wardetzky, E. Grinspun, *ACM Trans. Graphics* **2010**, *29*, 1.
[19] F. T. Peirce, *J. Textile Institute Trans.* **1930**, *21*, T377.
[20] M. K. Jawed, F. Da, J. Joo, E. Grinspun, P. M. Reis, *Proc. Natl. Acad. Sci. USA* **2014**, *111*, 14663.